analytical chemistry

pubs.acs.org/ac Article

Catalytic Hairpin Assembly-Driven Ratiometric Dual-Signal Electrochemical Biosensor for Ultrasensitive Detection of MicroRNA Based on the Ratios of Fe-MOFs and MB-GA-UiO-66-NH_2

Jiangbo Dong, Li Wen, Huisi Yang, Jiaying Zhao, Congjuan He, Zhikun Hu, Lan Peng, Changjun Hou,* and Danqun Huo*

Cite This: *Anal. Chem.* 2022, 94, 5846−5855 Read Online

ACCESS | Metrics & More | Article Recommendations | Supporting Information

ABSTRACT: In this work, a novel ratio electrochemical biosensing platform based on catalytic hairpin assembly target recovery to trigger dual-signal output was developed for ultrasensitive detection of microRNA (miRNA). To achieve the ratiometric dual-signal strategy, methylene blue (MB), an electrochemical indicator, was ingeniously loaded into the pores of graphene aerogel (GA) and metal−organic framework (MOF) composites with high porosity and large specific surface area, and another electrochemical indicator Fe-MOFs with distinct separation of redox potential was selected as a signal probe. Concretely, with the presence of the target miRNA, the CHA process was initiated and the signal probe was introduced to the electrode surface, producing abundant double-stranded H1-H2@Fe-MOFs-NH_2. Then, the measurement and analysis of the prepared ratiometric electrochemical biosensor by differential pulse voltammetry (DPV) showed that the introduction of the target miRNA led to an increase in the oxidation peak signal of Fe-MOFs (+0.8 V) and a decrease in the oxidation peak signal of MB (−0.23 V). Therefore, the peak current ratio of $I_{Fe\text{-}MOFs}/I_{MB}$ could be employed to accurately reflect the actual concentration of miRNA. Under optimal conditions, the detection limit of the proposed biosensor was down to 50 aM. It was worth noting that the proposed biosensor exhibited excellent detection performance in a complex serum environment and tumor cell lysates, showing great potential in biosensing and clinical diagnosis.

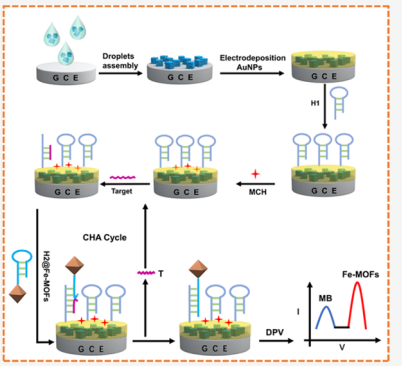

INTRODUCTION

MicroRNAs (miRNAs) have a crucial regulatory effect on biological processes of cell growth, proliferation, differentiation, and apoptosis.[1−4] Also, it has been demonstrated that cancer diseases and serious genetic-related diseases are closely related to the abnormal expression of miRNAs.[5,6] Therefore, there is an urgent need to develop an ultrasensitive miRNA detection method for clinical diagnosis. Although various traditional analytical techniques, including microarrays,[7] Northern blotting,[8] and fluorescence,[9] have shown satisfactory performance in miRNA detection, the drawbacks of high cost, complicated operation, and sample consumption still hinder their further development. To address the shortcomings, some other methods, such as electrochemiluminescence (ECL),[10] surface plasmon resonance,[11] and electrochemistry,[12] have been applied to the detection of miRNA. Among them, the electrochemical-based technique has ignited greater interest due to its advantages of handy operation, excellent selectivity, rapidness, and low cost.[13,14]

Despite its many merits, electrochemistry suffers from some of the following limitations. To our knowledge, most electrochemical sensors reported at present use a single electrochemical signal,[14,15] which may restrain the reproducibility, stability, and reliability of the sensors in detection. The main reason for this is that a single-signal output is easily interfered with by internal or external factors such as experimental environment, instrument state, etc.[16] However, the emergence of a ratiometric dual-signal strategy provides an intelligent choice for improving the performance of biosensors in practical applications. The ratiometric electrochemical sensor determines the analyte concentration by measuring the ratio of the peak current intensity of two electroactive probes with distinct redox potentials, which significantly improves the accuracy and reproducibility of the detection method through a built-in correction to the effect of inherent background signals.[17] It is worth pointing out that the selection of stable and noninterfering signal probes in ratiometric electrochemical sensors is particularly important. Currently, several classic electroactive organic small molecules, such as ferrocene (Fc), thionine (Thi), or methylene blue (MB), are

Received: December 7, 2021
Accepted: March 25, 2022
Published: April 5, 2022

https://doi.org/10.1021/acs.analchem.1c05293
Anal. Chem. 2022, 94, 5846−5855

Scheme 1. (A) Schematics of the MB-GA-UiO-66-NH_2 Synthesis Procedure and (B) Principle of the Ratiometric Electrochemical Biosensor for the Detection of miRNA-155

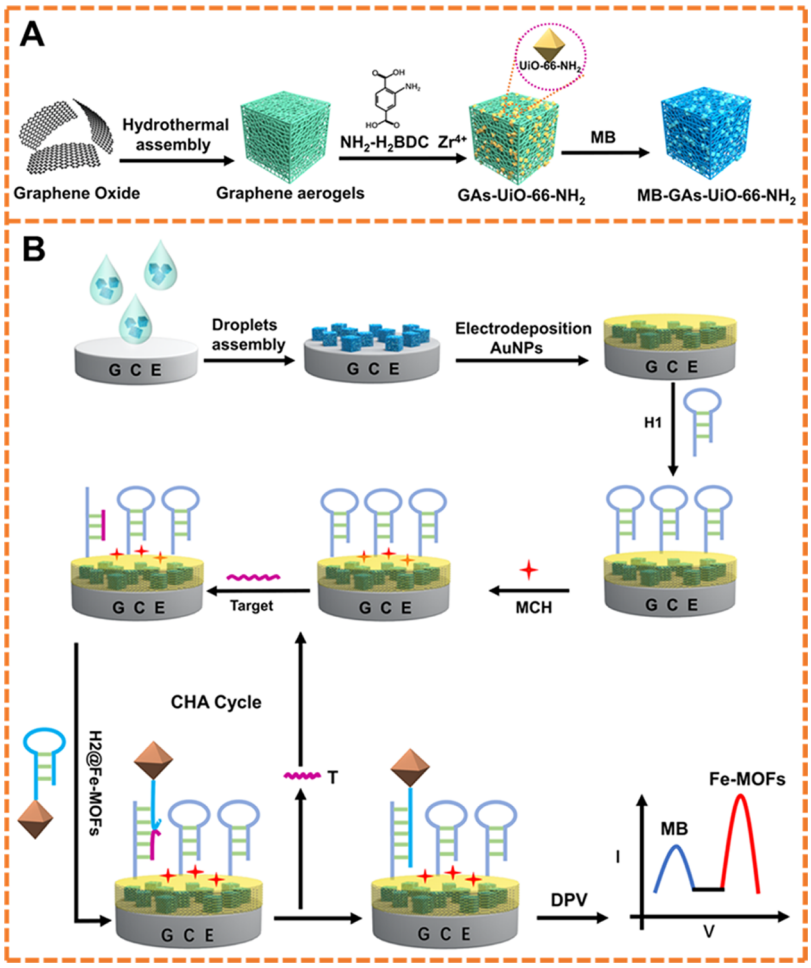

mainly used as electrochemical signal indicators.[18] Unfortunately, they easily come off the electrode surface. To solve the above issues, a popular strategy is to modify signal molecules (such as MB or Fc) on oligonucleotides to construct oligonucleotide-assisted ratio sensing, which undoubtedly causes complex operations and high costs.[19] In addition to the disadvantage that electroactive organic small molecules are difficult to immobilize, we also have to face the fact that their electroactivity is not strong enough.[20]

Recently, with the emergence of different nanomaterials, a feasible solution has been provided for the shortcomings of difficult immobilization and low electroactivity of electroactive organic small molecules. Among them, MOFs have attracted extensive attention due to their abundant channels, flexible porosity, and easy synthesis.[21] Given the high porosity of MOF nanomaterials, electroactive organic small molecules can be effectively accommodated and generate a sufficiently strong electroactive signal, which can greatly improve the performance of electrochemical sensors. Moreover, some MOFs (e.g., Fe-MOFs, Cu MOFs) are also used as electrochemical signal labels, which has been confirmed in some reports.[22,23] However, the direct application of MOFs in the electrochemical field is limited because of the poor conductivity. In this respect, the combination of MOF and conductive nanomaterials has been proven to be a potential method to enhance the conductivity of MOFs.[24] Up to now, various nanomaterials, including graphene,[25] MoS_2,[26] and conductive polymer,[27] have been introduced into MOFs. Graphene aerogels (GAs), a type of porous nanomaterial with high porosity, large surface area, and excellent electron-transfer ability, have been diversely applied in sensors, wearable devices, and catalysts.[28−30] The special structure of GAs offers multiple sites for the binding of MOFs. The result is that the coupling of MOFs into GAs not only keeps the intrinsic characteristic of two nanomaterials but also forms a synergy effect that is novel and interesting.[31]

Herein, we constructed a new ratiometric electrochemical biosensor to detect miRNA, in which GA-UiO-66-NH_2 loaded with a large amount of MB (MB-GA-UiO-66-NH_2) was used as the base material and Fe-MOFs were applied as the signal tags, combing with catalytic hairpin assembly (CHA) for target recycling. To verify this strategy, we used microRNA-155 (miRNA-155) as the detection object (Scheme 1). First, the GA-UiO-66-NH_2 composite materials with UiO-66-NH_2 growth in the framework of GAs were prepared by the solvothermal reaction. Particularly, the high porosity and large specific surface area of GA-UiO-66-NH_2 provided a platform for accommodating a large number of electroactive molecules MB. Then, a layer of AuNPs was electrodeposited on the surface of the prepared working electrode (MB-GA-UiO-66-NH_2/GCE) to fix the capture hairpin probe H1, which could also further improve the sensitivity of the sensing electrode.

https://doi.org/10.1021/acs.analchem.1c05293
Anal. Chem. 2022, 94, 5846−5855

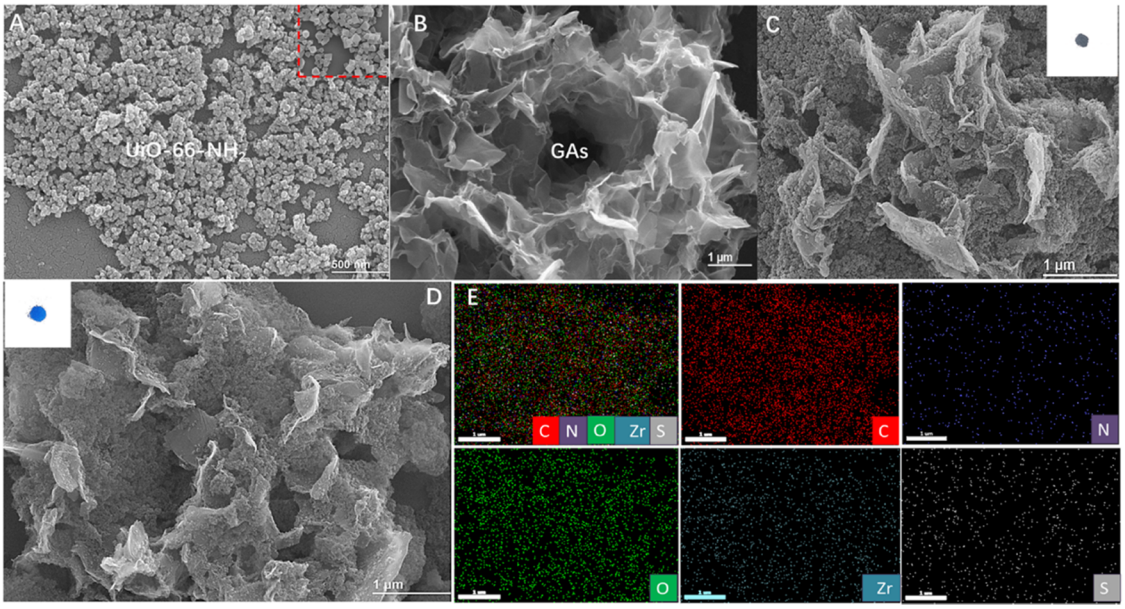

Figure 1. SEM images of (A) UiO-66-NH_2, (B) GAs, (C) GA-UiO-66-NH_2, and (D) MB-GA-UiO-66-NH_2. Insets in (C, D) were the photographs of the powers. The corresponding EDS elemental mapping data (E) of MB-GA-UiO-66-NH_2. Insets were the photographs.

With the help of miRNA-155, the hairpin structure of H1 was opened to form an H1-miRNA-155 intermediate. In the presence of another Fe-MOFs-NH_2-labeled hairpin H2 (H2@Fe-MOFs-NH_2), miRNA-155 was replaced to form an H1−H2 hybrid. The released target could be used to trigger another cycle, which was beneficial to signal enhancement. Finally, the current intensity ratio of the two signal indicators (reduced MB signal, enhanced Fe-MOF signal) reflected the concentration of miRNA-155. This work combined the advantages of catalytic hairpin assembly bio-amplification technology and ratiometric dual-signal strategy to achieve ultrasensitive and highly specific detection of miRNA, providing a universal and potential method for the detection of other markers in clinical diagnosis.

EXPERIMENTAL SECTION

Preparation of MB-GA-UiO-66-NH_2. The as-synthesized GA-UiO-66-NH_2 composites (20 mg) were dispersed into 15 mL of ultrapure water, followed by sonicating to obtain a homogeneous suspension. Subsequently, 10 mg of MB were charged into the mixed solution and stirred for 24 h vigorously. Finally, the above solution was centrifuged, washed three times with ultrapure water, and kept at 4 °C for the subsequent experiment.

Preparation of H2@Fe-MOFs-NH_2 Nanoprobes. The prepared Fe-MOFs-NH_2 particles (15 mg) were dispersed in 5 mL of PBS (10 mM, pH = 7.4) containing 2.5% glutaraldehyde and shaken for 4 h. Following that, to remove excess glutaraldehyde, the suspension was washed several times with PBS. After that, the products (500 μL) were incubated with 50 μL of amino-functionalized Hairpin probe H2 (NH_2-H2, 50 μM) for 12 h at 4 °C. Finally, the H2@Fe-MOFs-NH_2 nanoprobes were centrifuged to remove unbound Hairpin probe H2 and redispersed in 500 μL of PBS.

Fabrication of the Ratiometric Electrochemical Biosensor. Generally, 6 μL of MB-GA-UiO-66-NH_2 (1.5 mg mL^{-1}) was dropped onto a bare GCE polished by 30 and 50 nm alumina powder, followed by drying at room temperature. Thereafter, AuNPs were electrodeposited on MB-GA-UiO-66-NH_2/GCE in a 5 mM $HAuCl_4$ solution to obtain AuNPs/MB-GA-UiO-66-NH_2/GCE. After that, 0.5 μM of H1 was pipetted onto the AuNPs/MB-GA-UiO-66-NH_2/GCE and reacted for 2 h at 37 °C. Furthermore, 5 μL of 1 mM MCH was dropped on the aforementioned modified electrode and incubated for 30 min to block the unbound sites. Finally, 6 μL of different concentrations of miRNA-155 and 6 μL of H2@Fe-MOFs-NH_2 nanoprobes were incubated on MCH/H1/AuNPs/MB-GA-UiO-66-NH_2/GCE at 37 °C for 120 min. In each step, the modified GCE was rinsed several times with PBS buffer to prevent unbound and weakly bound materials.

Electrochemical Measurements. CV and EIS were recorded in a 5 mM $[Fe(CN)_6]^{3-/4-}$ solution containing 0.1 M KCl. The electrodeposition procedure was carried out at a potential of −0.2 V for 120 s. Differential pulse voltammetry (DPV) was monitored at 0.1 M PBS (pH = 7.4), and the related parameters were as follows: pulse amplitude, 50 mV; pulse width, 0.05 s; and pulse period, 0.2 s.

Other experimental details were described in the Supporting Information.

RESULTS AND DISCUSSION

Characterization of the Prepared Nanomaterials. The morphology and structure of the materials were characterized by scanning electron microscopy (SEM). The SEM result (Figure 1A) of UiO-66-NH_2 proved that the prepared UiO-66-NH_2 crystals possessed a regular octahedron-like morphology, which was in good agreement with previous reports.[32] As depicted in Figure 1B, the GAs had a crisscross network structure and various active sites, which was convenient for compounding with other nanomaterials. After GAs was combined with UiO-66-NH_2, we could clearly observe that the GAs was the main framework of the composite material, and UiO-66-NH_2 particles grew in situ in the GAs matrix (Figure 1C), which confirmed that the successful preparation of GA-UiO-66-NH_2 composites. After loading the electroactive indicator (MB) into GA-UiO-66-NH_2, the SEM image was

https://doi.org/10.1021/acs.analchem.1c05293
Anal. Chem. 2022, 94, 5846−5855

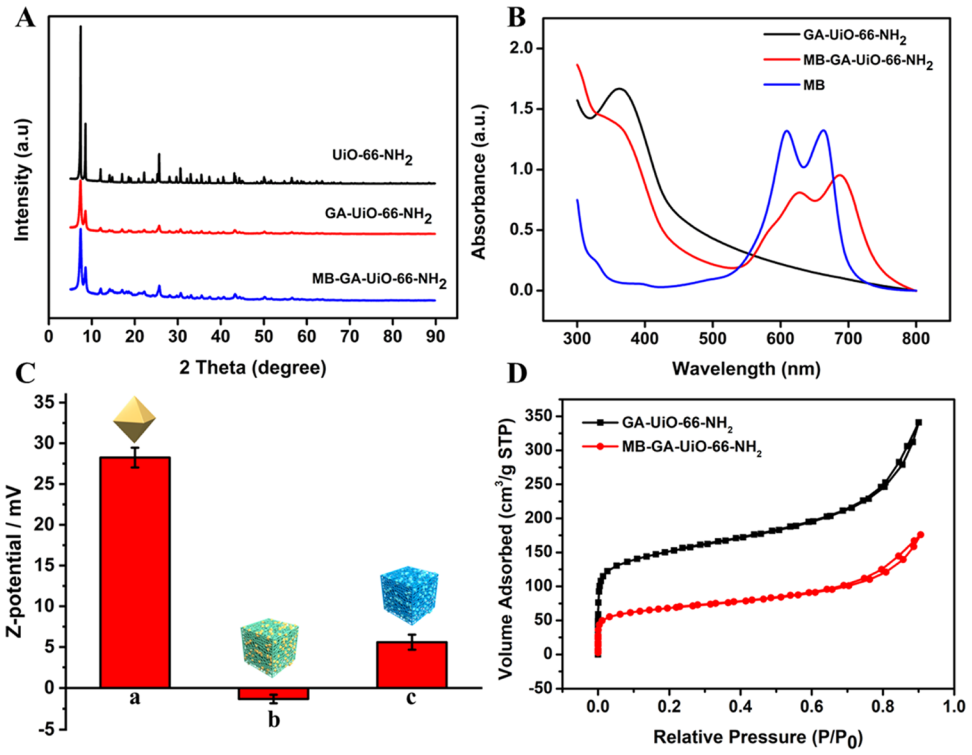

Figure 2. (A) XRD patterns of UiO-66-NH_2, GA-UiO-66-NH_2, and MB-GA-UiO-66-NH_2. (B) Ultraviolet−visible (UV−vis) absorption spectra and (C) ζ-potentials of (a) UiO-66-NH_2, (b) GA-UiO-66-NH_2, and (c) MB-GA-UiO-66-NH_2. (D) N_2 adsorption−desorption isotherms of the prepared materials.

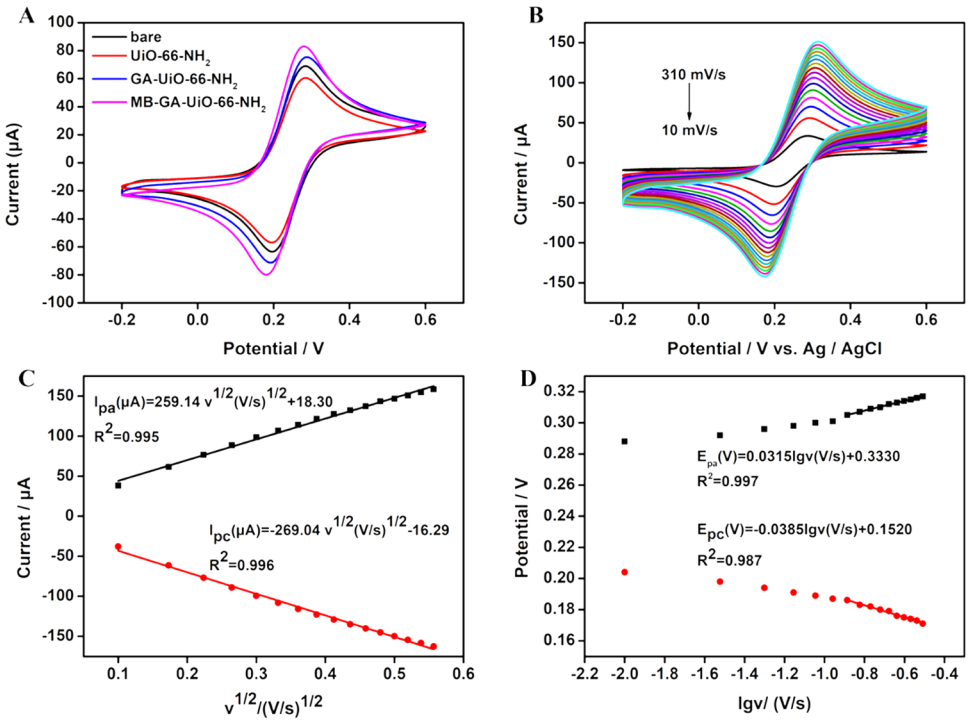

Figure 3. (A) CV curves of bare GCE, UiO-66-NH_2, GA-UiO-66-NH_2, MB-GA-UiO-66-NH_2, and GA-modified GCE in 5 mM $[Fe(CN)_6]^{3-/4-}$ containing 0.1 M KCl. (B) CV curves of MB-GA-UiO-66-NH_2/GCE at different scan rates in 5 mM $[Fe(CN)_6]^{3-/4-}$ containing 0.1 M KCl. (C) Linear relationship between the anodic and cathodic peak currents versus scan rate. (D) Fitting straight curves of the lgv versus potential.

almost consistent with that of GA-UiO-66-NH_2 except for the color change (Figure 1D). Moreover, the corresponding EDS elemental mappings (Figure 1E) were carried out to observe the elemental compositions of MB-GA-UiO-66-NH_2, in which the S signal confirmed the successful loading of the MB in the GA-UiO-66-NH_2 structure.

The X-ray diffraction (XRD) patterns of the prepared nanomaterials are depicted in Figure 2A. The sharp diffraction

https://doi.org/10.1021/acs.analchem.1c05293
Anal. Chem. 2022, 94, 5846−5855

peaks of UiO-66-NH_2 crystals were matched with the previous study,[21] indicating the successful preparation and excellent crystallinity of UiO-66-NH_2. After GAs and MB were successively introduced, the XRD dates of GA-UiO-66-NH_2 and MB-GA-UiO-66-NH_2 preserved all diffraction peaks, suggesting that the crystal structure and integrity of UiO-66-NH_2 were maintained. The UV−vis date of nanocomposites is shown in Figure 2B. The peak at 664 nm was considered the characteristic absorption peak of MB,[33] while GA-UiO-66-NH_2 had no characteristic absorption peak within the measurement wavelength range. However, after the combination of GA-UiO-66-NH_2 and MB, the characteristic absorption peak of MB-GA-UiO-66-NH_2 could be clearly observed, demonstrating the successful loading of MB. To further verify the successful formation of the nanocomposites, a ζ-potential analysis was conducted. As shown in Figure 2C, the ζ-potential value of UiO-66-NH_2 decreased from +28.25 to −1.32 mV after conjugation with negatively charged GAs.[34] After GA-UiO-66-NH_2 was modified with cationic dye MB,[35] the potential increased to +5.59 mV, which further proved that MB was wrapped in GA-UiO-66-NH_2. Furthermore, the adsorption−desorption isotherm (Figure 2D) also demonstrated the effective encapsulation of MB in GA-UiO-66-NH_2. The BET surface areas of GA-UiO-66-NH_2 and MB-GA-UiO-66-NH_2 were 680.24 and 240.32 $m^2\ g^{-1}$, respectively. These results strongly proved the successful synthesis of MB-GA-UiO-66-NH_2.

In addition, Fe-MOF-NH_2 was characterized by SEM, X-ray photoelectron spectroscopy (XPS), and XRD, and the details are in Figure S2.

Electrochemical Property of MB-GA-UiO-66-NH_2. The property of materials was very important for the preparation of ratiometric electrochemical sensors. As depicted in Figure 3A, the electrochemical performances of electrodes modified with different nanomaterials were compared by CV. Compared with the bare GCE and UiO-66-NH_2/GCE, the redox peak signal of the GA-UiO-66-NH_2/GCE increased due to the more abundant electron-transfer channels of the prepared composites. Furthermore, we could clearly observe that in the CV curves of GA-UiO-66-NH_2/GCE and MB-GA-UiO-66-NH_2/GCE, the redox peak signal of the latter was larger. The above results could be attributed to the fact that the introduction of MB with high electroactivity further accelerated the electron transfer on the electrode surface, which indicated that MB-GA-UiO-66-NH_2 had excellent electronic conductivity. Moreover, we calculated the electroactive surface area (A) by the Randles−Sevcik equation.[36]

$$I_p = 2.69 \times 10^5 \times n^{3/2} A D^{1/2} v^{1/2} C \quad (1)$$

According to eq (1), the electroactive surface area of MB-GA-UiO-66-NH_2/GCE (0.204 cm^2) increased by 1.3 times, 1.5 times, and 1.8 times compared with that of GA-UiO-66-NH_2/GCE (0.172 cm^2), GCE (0.143 cm^2), and UiO-66-NH_2/GCE (0.121 cm^2), respectively, which proved the satisfactory performance of MB-GA-UiO-66-NH_2 again.

As displayed in Figure 3B, the peak current increased linearly as the scan rate increased, and the relevant linear regression equations are shown in Figure 3C: where the anode is I_{pa} (μA) = 259.14 $v^{1/2}$ + 18.30 (R^2 = 0.995) and the cathode is I_{pc} (μA) = −269.04 $v^{1/2}$ −16.29 (R^2 = 0.996), showing that the oxidation−reduction reaction at the interface of the modified electrode was a diffusion-controlled process. Moreover, the rapid electron-transfer rate was beneficial to enhance the current signal. As shown in Figure 3D, with the increase in the scan rate, the peak potential difference (ΔE_p) between the anode and cathode gradually increased, indicating that the irreversibility of the electrode process increased. When ΔE_p > 0.12 V, the linear equations were E_{pa} (V) = 0.0315 lg(v) + 0.3330 (R^2 = 0.997) and E_{pc} (V) = −0.0385 lg(v) + 0.1520 (R^2 = 0.987), respectively. In addition, based on the Laviron theory,[37] we further calculated the k_s (apparent electron transfer rate constant), which could be used to evaluate the electron-transfer rate.

$$\lg\frac{k_a}{k_c} = \lg\frac{\alpha}{1-\alpha} \quad (2)$$

$$\lg k_s = \alpha\lg(1-\alpha) + (1-\alpha)\lg\alpha - \lg\left(\frac{RT}{nFv}\right) - \frac{2.3RT\alpha}{(1-\alpha)nF\Delta k_p} \quad (3)$$

According to (eqs 2) and (3), α = 0.45 (charge transfer coefficient) and k_s = 1.201 s^{-1}. The k_s was larger than that reported in these articles (Table S2), which showed that MB-GA-UiO-66-NH_2 accelerated the electron transfer.

Verification of CHA Amplification Strategy. The feasibility of the CHA amplification strategy was crucial to the construction of the sensor, which was verified by polyacrylamide gel electrophoresis (PAGE). As shown in Figure 4, lanes 1−4 corresponded to H1, H2, miRNA-155 (T), and H1/H2 mixture, respectively. As planned, CHA amplification was not triggered without target miRNA-155. However, when the target was incubated with H1/H2, a new band appeared in lane 5, indicating the successful triggering of the CHA program.

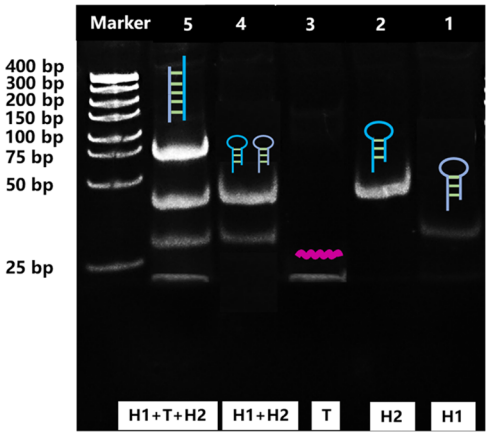

Figure 4. Native PAGE showing the CHA strategy: lane 1, H1; lane 2, H2; lane 3, miRNA-155 (T); lane 4, mixture of H1 and H2; and lane 5, mixture of H1, miRNA-155 (T), and H2. The native PAGE (12%) was typically run at 110 V for 60 min in 1× TBE.

Electrochemical Characterization of Ratiometric Electrochemical Biosensor Fabrication. The preparation process of the ratiometric electrochemical biosensor was characterized by CV and EIS. As shown in Figure S3A, MB-GA-UiO-66-NH_2-modified GCE (curve b) exhibited a larger redox peak than bare GCE (curve a), suggesting that MB-GA-UiO-66-NH_2 had excellent electron-transfer ability. After AuNPs were electrodeposited on MB-GA-UiO-66-NH_2/GCE, the redox peak (curve c) further increased because of

https://doi.org/10.1021/acs.analchem.1c05293
Anal. Chem. 2022, 94, 5846−5855

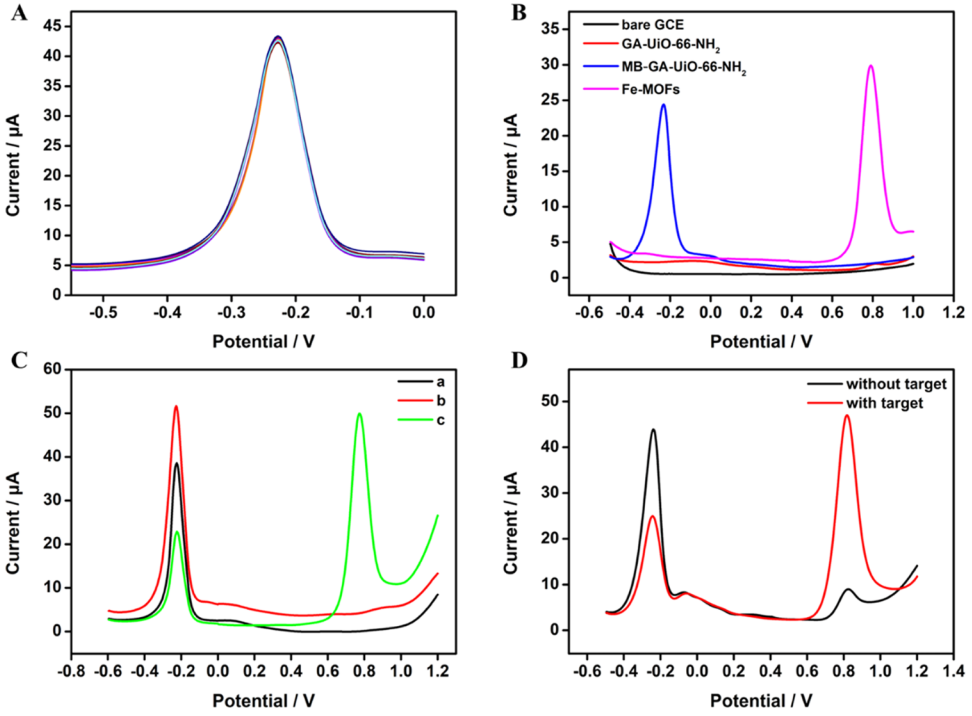

Figure 5. (A) Repeating the measured DPV response of MB-GA-UiO-66-NH_2/GCE 10 times. (B) DPV responses of different modified electrodes. (C) DPV responses of MB-GA-UiO-66-NH_2/GCE (a), AuNPs/MB-GA-UiO-66-NH_2/GCE (b), and H2@Fe-MOFs-NH_2/MCH/H1/AuNPs/MB-GA-UiO-66-NH_2/GCE (c). (D) DPV responses of MB and Fe-MOFs in the absence and presence of 0.1 μM miRNA-155. All DPV responses were measured in 0.1 M PBS buffer solution (pH 7.4). The related parameters were as follows: pulse amplitude, 50 mV; pulse width, 0.05 s; and pulse period, 0.2 s.

the high electrical conductivity of AuNPs. Then, when H1 was self-assembled on AuNPs/MB-GA-UiO-66-NH_2/GCE, the peak current decreased obviously (curve d), which could be attributed to the repulsion effect between the negatively charged DNA molecules and the negatively charged $[Fe(CN)_6]^{3-/4-}$. Subsequently, MCH, as an insulating layer, was loaded on the modified electrode, and the peak signal further decreased (curve e). Finally, the target miRNA-155 and H2@Fe-MOFs-NH_2 (curve f) were introduced to initiate the CHA program to form a double-stranded nanoprobe with a negative charge density, resulting in the weakening of the current intensity again. These results proved the successful manufacture of the sensing platform.

EIS was also used to record the fabrication of the biosensor, and the corresponding equivalent circuit is inserted in Figure S3B. The R_{ct} of MB-GA-UiO-66-NH_2-modified GCE (curve b, 136 Ω) was smaller than of the bare GCE (curve a, 220 Ω), which was attributed to the excellent conductivity of MB-GA-UiO-66-NH_2 composite materials. Then, R_{ct} further decreased (curve c, 74 Ω) after AuNPs were electrodeposited on MB-GA-UiO-66-NH_2/GCE. However, when H1 (curve d, 173 Ω) and MCH (curve e, 390 Ω) were stepwise modified onto AuNPs/MB-GA-UiO-66-NH_2/GCE, the R_{ct} increased in turn. As expected, the R_{ct} increased again after CHA amplification was triggered (curve f, 470 Ω). The above results were consistent with the CVs, which proved that the construction of the miRNA detection platform was successful again.

Investigation of the Feasibility of the Ratiometric Electrochemical Sensor Detection. To confirm the feasibility of the constructed ratio sensor in miRNA detection, a set of DPV experiments was carried out. First, the stability of MB-GA-UiO-66-NH_2 as the substrate played a vital role in the entire experiment. As depicted in Figure 5A, 10 measurements of DPV showed similar results, which indicated the excellent stability of MB-GA-UiO-66-NH_2. Then, to verify the feasibility of MB-GA-UiO-66-NH_2 and Fe-MOFs as electroactive probes, the electrodes modified by GA-UiO-66-NH_2, MB-GA-UiO-66-NH_2, and Fe-MOFs were studied by DPV. As shown in Figure 5B, almost no current signals were generated when the bare GCE and GA-UiO-66-NH_2/GCE were measured by DPV experiments. However, when the signals of MB-GA-UiO-66-NH_2/GCE and Fe-MOFs/GCE were recorded by DPV, a pair of distinctly separated oxidation potentials appeared at −0.23 V (MB) and +0.8 V (Fe-MOFs).

To explore the reason that the DPV response of MB decreased in ratio analysis strategy, a series of controlled experiments were performed, as displayed in Figure 5C. The DPV signal of MB-GA-UiO-66-NH_2/GCE was about 35.95 μA, while that of AuNPs/MB-GA-UiO-66-NH_2/GCE increased to 45.68 μA, which could be attributed to the fact that AuNPs with excellent conductivity enhanced the electron transfer. With the layer-by-layer modification of H1, MCH, miRNA-155, and H2@Fe-MOFs-NH_2, the DPV signal of H2@Fe-MOFs-NH_2/MCH/H1/AuNPs/MB-GA-UiO-66-NH_2/GCE decreased. This was because the negatively charged DNA, nonconductive MCH, and poorly conductive nanoprobes occupied and blocked the electron transmission channels, and hindered the transfer of electrons, thus decreasing the DPV response of MB. Furthermore, the DPV responses of MB and Fe-MOFs were measured in the presence and absence of the target miRNA-155. As displayed in Figure 5D, when target miRNA-155 was present, the DPV responses of MB and Fe-MOFs were 20.01 and 45.60 μA, respectively, and the $I_{Fe\text{-}MOFs}/I_{MB}$ value was 2.28. However, in the absence

https://doi.org/10.1021/acs.analchem.1c05293
Anal. Chem. 2022, 94, 5846−5855

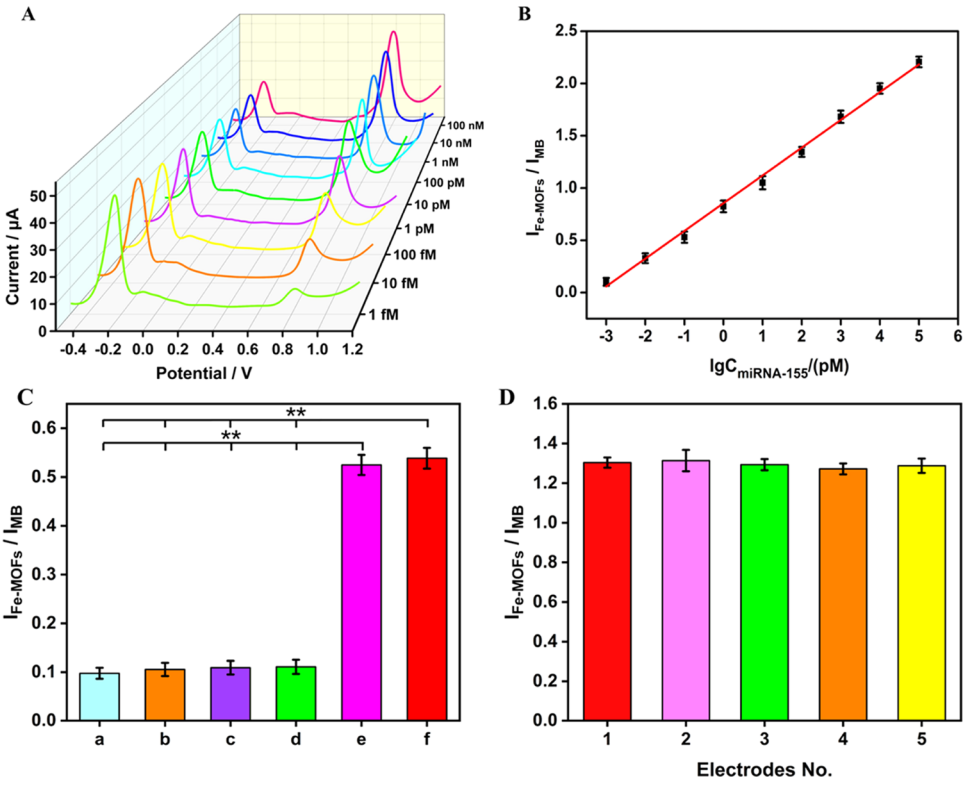

Figure 6. (A) DPV of the proposed biosensor under different miRNA-155 concentrations. (B) Linear relation of $I_{Fe\text{-}MOFs}/I_{MB}$ values and the logarithm of target miRNA-155. (C) Selectivity investigation of the biosensor (a → f, blank sample, 100 fM let-7a, 100 fM miRNA-21, 100 fM noncomplementary sequence (NC), 100 fM miRNA-155, mixture of forenamed miRNA with the same concentration of 100 fM). Asterisks represent the statistically significant differences (**$p < 0.01$). (D) $I_{Fe\text{-}MOFs}/I_{MB}$ of independently fabricated five biosensors, the concentration of miRNA-155 was 50 pM. All DPV responses were measured in 0.1 M PBS buffer solution (pH 7.4). Error bars represented standard deviations of three parallel experiments.

of the target, a strong MB signal was observed, and a weak Fe-MOFs signal was also detected due to physical adsorption. The above results confirmed the feasibility of detecting miRNA based on the proposed ratio strategy.

Optimization of the Experimental Conditions. To achieve the best detection performance of the constructed biosensor, some important experimental parameters were optimized, including the concentration of MB-GA-UiO-66-NH_2, the electrodeposition time of AuNPs, the self-assembly time of H1 on the modified electrode, and the catalytic hairpin assembly time. Detailed descriptions are shown in Figure S4.

Analytical Performance of the Ratiometric Electrochemical Biosensor. Under optimal experimental conditions, the as-proposed electrochemical biosensor was employed to detect different concentrations of miRNA-155. As shown in Figure 6A, the signal of MB gradually decreased and that of Fe-MOFs increased with the increase in miRNA-155 concentration from 1 fM to 100 nM. A good linear relationship between the ratio value of Fe-MOFs and MB and the logarithm of the miRNA-155 concentration could be seen in Figure 6B, and the linear regression equation was $I_{Fe\text{-}MOFs}/I_{MB} = 0.265 \lg C_{miRNA\text{-}155}/(\text{pM}) + 0.855$ ($R^2 = 0.997$) with the detection limit of 50 aM (S/N = 3). By comparing the ratio dual-signal strategy with the single-signal strategy, the as-prepared biosensor showed a wider detection range and a lower detection limit than only the MB-GA-UiO-66-NH_2 sensor system (100 fM−10 nM, LOD = 1.5 fM; Figure S5A,B) and only the Fe-MOFs sensor system (10 fM−10 nM, LOD = 0.8 fM; Figure S5C,D). The analysis performance of the prepared biosensor was comparable to or better than that of previous methods in the detection range and detection limit (Table 1). The excellent performance of the ratiometric electrochemical biosensor could be attributed to the following points: (1) MB was ingeniously loaded into the pores of GAs-UiO-66-NH_2, which not only formed composites with high electroactive surface area but also accelerated the electron transfer and improved analytical sensitivity; (2) the MB and Fe-MOFs with distinctly separated and interference-free redox potentials ensured the successful design of the ratiometric electrochemical sensor; (3) the CHA target recovery strategy provided exponential amplification, which was beneficial to enhance the signal; and (4) the ratiometric dual-signal method

Table 1. Analytical Performance Compared with Other Works for miRNA Detection

detection modes	target	linear range	detection limit	refs
electrochemistry	miRNA-155	0.8 fM−1 nM	0.35 fM	38
ECL	miRNA-21	1 fM−100 pM	0.1 fM	39
electrochemistry	miRNA-21	1 pM−10 nM	0.26 pM	40
electrochemistry	miRNA-141	1 fM−100 pM	200 aM	13
SERS	miRNA-155	100 fM−5 nM	1.5 fM	41
PEC	miRNA-21	1 fM−1 nM	0.41 fM	42
ECL	miRNA-122	100 aM−1 pM	82 aM	43
electrochemistry	miRNA-21	1 fM−1 nM	0.29 fM	44
electrochemistry	miRNA-155	1 fM−100 nM	50 aM	this work

https://doi.org/10.1021/acs.analchem.1c05293
Anal. Chem. 2022, 94, 5846−5855

surmounted the inherent systematic error, significantly improving the accuracy and reproducibility of the biosensor.

Specificity, Reproducibility, and Stability. Some other potential interfering miRNAs were used to evaluate the specificity of the as-prepared biosensing platform. As shown in Figure 6C, the $I_{Fe\text{-}MOFs}/I_{MB}$ values of 0.097, 0.105, 0.109, 0.111, 0.525, and 0.539 were obtained in the measurement of blank, 100 fM let-7a, 100 fM miRNA-21, 100 fM NC, 100 fM miRNA-155, and mixture of the same concentration. Notably, only in the prsence of the target miRNA-155, the biosensor showed an obvious electrochemical signal, which was about 5 times that of the current response of the control groups (blank, let-7a, miRNA-21, NC). The results showed that only the perfectly matched sequence could trigger signal amplification strategies, indicating that the proposed biosensor possessed superior selectivity and specificity toward target miRNA-155.

To check the reproducibility of the ratiometric electrochemical biosensor, five biosensors were prepared by the same procedure for the detection of 50 pM miRNA-155. As exhibited in Figure 6D, the current responses of five biosensors were similar, and the relative standard deviation (RSD) was only 1.4%, manifesting that the reproducibility was acceptable. Furthermore, the stability of the constructed biosensor was also tested. As displayed in Figure S6, the $I_{Fe\text{-}MOFs}/I_{MB}$ value could retain nearly 97% original signal after 20 days, indicating that the proposed biosensor possessed good stability.

Real Sample Analysis. To assess the application potential of the prepared biosensing platform, different concentrations of miRNA-155 (1, 10, 100 pM) were added to human serum samples diluted 10-fold with 0.01 M (pH = 7.4) PBS for the analysis of the spiked experiment. Specifically, 6 μl of diluted serum containing various concentrations of miRNA-155 were incubated on the electrodes, and the DPV responses at −0.23 V and +0.8 V potentials were recorded. The $I_{Fe\text{-}MOFs}/I_{MB}$ value was finally converted to the molar concentration of miRNA-155 by comparing with the standard linear calibration curve to calculate the recovery. As displayed in Table S3, the RSD of the prepared biosensor was less than 2.38% and the recovery was between 93.34 and 104.20%, indicating that the prepared biosensor platform had good accuracy in clinical analysis. Furthermore, the developed sensor was employed to detect miRNA-155 extracted from HUVECs (human umbilical vein endothelial cells), MCF-7, and HeLa cells to further verify its practicable application. As shown in Figure 7, the $I_{Fe\text{-}MOFs}/I_{MB}$ value of the lysates extracted from HUVECs had a low response and slow growth for miRNA-155 detection. On the contrary, with the increasing number of MCF-7 cells and HeLa cells from 1×10^2 to 1×10^4, the $I_{Fe\text{-}MOFs}/I_{MB}$ value obviously increased for miRNA-155. At the same time, the $I_{Fe\text{-}MOFs}/I_{MB}$ values of miRNA-155 in MCF-7 cells and HeLa cells were conspicuously higher than those of normal cells, indicating the overexpression of miRNA-155 in the MCF-7 and HeLa cells.[45−47]

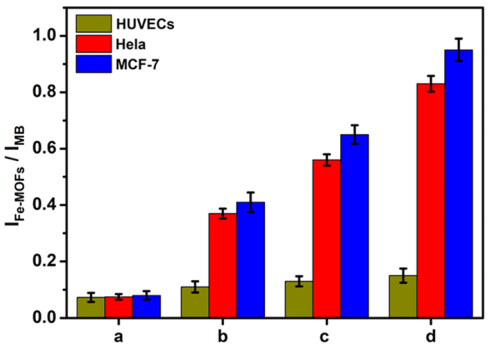

Figure 7. Detection of miRNA-155 from HUVECs, HeLa, and MCF-7 cells (from a−d: bank, 10^2, 10^3, and 10^4).

CONCLUSIONS

In summary, an ultrasensitive ratiometric electrochemical biosensor was constructed for miRNA-155 detection. To our knowledge, this was the first time that MB was ingeniously loaded into the pores of GAs-UiO-66-NH_2 to provide a stable and powerful electrochemical signal. Moreover, Fe-MOFs, another electroactive probe, were introduced via CHA target recovery. By making full use of the distinctly separated redox potential of the MB and Fe-MOFs, the elaborately designed biosensor could quantify the level of miRNA-155 based on the $I_{Fe\text{-}MOFs}/I_{MB}$ value in the range of 1 fM−100 nM, and the detection limit was as low as 50 aM. Furthermore, the ratiometric electrochemical biosensor also had favorable reproducibility, long-term stability, and satisfactory recovery. More importantly, this newly designed strategy provided an applicable and universal platform for the detection of other tumor markers.

ASSOCIATED CONTENT

Supporting Information

The Supporting Information is available free of charge at https://pubs.acs.org/doi/10.1021/acs.analchem.1c05293.

Additional information as noted in the text; chemicals and apparatus, synthesis of GA, synthesis of UiO-66-NH_2, synthesis of GA-UiO-66-NH_2, synthesis of Fe-MOFs-NH_2, PAGE gel electrophoresis, all DNA and miRNA sequences used in this work, SEM images of UiO-66-NH_2, characterization of the Fe-MOF-NH_2, comparison of the apparent electron-transfer rate constant (k_s) with previous studies, electrochemical characterization of ratiometric electrochemical biosensor fabrication, optimization of the experimental conditions, comparison of ratio two-signal strategy and single-signal strategy, the stability of biosensor, and analysis of the spiked experiment (PDF)

AUTHOR INFORMATION

Corresponding Authors

Changjun Hou − *Key Laboratory for Biorheological Science and Technology of Ministry of Education, State and Local Joint Engineering Laboratory for Vascular Implants, Bioengineering College of Chongqing University, Chongqing 400044, P. R. China; National Facility for Translational Medicine (Shanghai), Shanghai 200240, P. R. China;* orcid.org/0000-0002-3608-116X; Phone: +86 23 6511 2673; Email: houcj@cqu.edu.cn; Fax: +86 23 6510 2507

Danqun Huo − *Key Laboratory for Biorheological Science and Technology of Ministry of Education, State and Local Joint Engineering Laboratory for Vascular Implants, Bioengineering College of Chongqing University, Chongqing 400044, P. R. China; Chongqing Key Laboratory of Bio-perception & Intelligent Information Processing, School of Microelectronics and Communication Engineering, Chongqing University, Chongqing 400044, P. R. China;* Email: huodq23@163.com

https://doi.org/10.1021/acs.analchem.1c05293
Anal. Chem. 2022, 94, 5846−5855

Authors

Jiangbo Dong − *Key Laboratory for Biorheological Science and Technology of Ministry of Education, State and Local Joint Engineering Laboratory for Vascular Implants, Bioengineering College of Chongqing University, Chongqing 400044, P. R. China*

Li Wen − *Key Laboratory for Biorheological Science and Technology of Ministry of Education, State and Local Joint Engineering Laboratory for Vascular Implants, Bioengineering College of Chongqing University, Chongqing 400044, P. R. China*

Huisi Yang − *Key Laboratory for Biorheological Science and Technology of Ministry of Education, State and Local Joint Engineering Laboratory for Vascular Implants, Bioengineering College of Chongqing University, Chongqing 400044, P. R. China*

Jiaying Zhao − *Key Laboratory for Biorheological Science and Technology of Ministry of Education, State and Local Joint Engineering Laboratory for Vascular Implants, Bioengineering College of Chongqing University, Chongqing 400044, P. R. China*

Congjuan He − *Key Laboratory for Biorheological Science and Technology of Ministry of Education, State and Local Joint Engineering Laboratory for Vascular Implants, Bioengineering College of Chongqing University, Chongqing 400044, P. R. China*

Zhikun Hu − *Key Laboratory for Biorheological Science and Technology of Ministry of Education, State and Local Joint Engineering Laboratory for Vascular Implants, Bioengineering College of Chongqing University, Chongqing 400044, P. R. China*

Lan Peng − *Chongqing Medical and Pharmaceutical College Basic Department, Chongqing 401331, P. R. China*

Complete contact information is available at: https://pubs.acs.org/10.1021/acs.analchem.1c05293

Notes

The authors declare no competing financial interest.

■ ACKNOWLEDGMENTS

This work was supported by the National Natural Science Foundation of China (No. 81772290), the Graduate Scientific Research and Innovation Foundation of Chongqing, China (CYS21069), the Fundamental Research Funds for the Central Universities (2021CDJYGRH006), the National Facility for Translational Medicine (Shanghai) Open Research Found (TMSK-2021-113), the Science and Technology Research Program of Chongqing Education Commission of China (KJCXZD2020006 and KJCXZD2020008), the Chongqing Graduate Tutor Team Construction Project, Analytical and Testing Center of Chongqing University (for FE-SEM/XPS/XRD/BET), and the sharing fund of Chongqing University's large equipment.

■ REFERENCES

(1) Bartel, D. P. *Cell* **2004**, *116*, 281−297.
(2) Ambros, V. *Nature* **2004**, *431*, 350−355.
(3) Gregory, R. I.; Yan, K. P.; Amuthan, G.; Chendrimada, T.; Doratotaj, B.; Cooch, N.; Shiekhattar, R. *Nature* **2004**, *432*, 235−240.
(4) Chan, J. A.; Krichevsky, A. M.; Kosik, K. S. *Cancer Res.* **2005**, *65*, 6029−6033.
(5) Dong, H.; Lei, J.; Ding, L.; Wen, Y.; Ju, H.; Zhang, X. *Chem. Rev.* **2013**, *113*, 6207−6233.
(6) Croce, C. M. *Nat. Rev. Genet.* **2009**, *10*, 704−714.
(7) Lee, J. M.; Jung, Y. *Angew. Chem., Int. Ed.* **2011**, *50*, 12487−12490.
(8) Pall, G. S.; Codony-Servat, C.; Byrne, J.; Ritchie, L.; Hamilton, A. *Nucleic Acids Res.* **2007**, *35*, e60.
(9) Zhuang, Y.; Huang, F.; Xu, Q.; Zhang, M.; Lou, X.; Xia, F. *Anal. Chem.* **2016**, *88*, 3289−3294.
(10) Xia, L. Y.; Li, M. J.; Wang, H. J.; Yuan, R.; Chai, Y. Q. *Anal. Chem.* **2020**, *92*, 14550−14557.
(11) Liu, X.; Huang, R.; Su, R.; Qi, W.; Wang, L.; He, Z. *ACS Appl. Mater. Interfaces* **2014**, *6*, 13034−13042.
(12) Cheng, F. F.; He, T. T.; Miao, H. T.; Shi, J. J.; Jiang, L. P.; Zhu, J. J. *ACS Appl. Mater. Interfaces* **2015**, *7*, 2979−2985.
(13) Zhou, Q. Y.; Ma, R. N.; Hu, C. L.; Sun, F.; Jia, L. P.; Zhang, W.; Shang, L.; Xue, Q. W.; Jia, W. L.; Wang, H. S. *Analyst* **2021**, *146*, 2705−2711.
(14) Qi, H.; Li, H.; Li, F. *Anal. Chem.* **2021**, *93*, 7739−7745.
(15) Zhao, Y.; Cui, L.; Sun, Y.; Zheng, F.; Ke, W. *ACS Appl. Mater. Interfaces* **2019**, *11*, 3474−3481.
(16) Xia, N.; Wang, X.; Zhou, B.; Wu, Y.; Mao, W.; Liu, L. *ACS Appl. Mater. Interfaces* **2016**, *8*, 19303−19311.
(17) Zhang, J.; Wang, D.; Li, Y. *ACS Appl. Mater. Interfaces* **2019**, *11*, 13557−13563.
(18) Miao, J.; Du, K.; Li, X.; Xu, X.; Dong, X.; Fang, J.; Cao, W.; Wei, Q. *Biosens. Bioelectron.* **2021**, *171*, 112713.
(19) Wang, X.; Liu, G.; Qi, Y.; Yuan, Y.; Gao, J.; Luo, X.; Yang, T. *Anal. Chem.* **2019**, *91*, 12006−12013.
(20) Tang, Z.; Ma, Z. *Sci. Rep.* **2016**, *6*, No. 35440.
(21) Zhao, Y.; Liu, H.; Shi, L.; Zheng, W.; Jing, X. *Sens. Actuators, B.* **2020**, *315*, 128155.
(22) Sun, Z.; Wang, L.; Wu, S.; Pan, Y.; Dong, Y.; Zhu, S.; Yang, J.; Yin, Y.; Li, G. *Anal. Chem.* **2020**, *92*, 3819−3826.
(23) Liu, T. Z.; Hu, R.; Zhang, X.; Zhang, K. L.; Liu, Y.; Zhang, X. B.; Bai, R. Y.; Li, D.; Yang, Y. H. *Anal. Chem.* **2016**, *88*, 12516−12523.
(24) Xie, F.-T.; Zhao, X.-L.; Chi, K.-N.; Yang, T.; Hu, R.; Yang, Y.-H. *Anal. Chim. Acta* **2020**, *1135*, 123−131.
(25) Wang, X.; Wang, Q.; Wang, Q.; Gao, F.; Gao, F.; Yang, Y.; Guo, H. *ACS Appl. Mater. Interfaces* **2014**, *6*, 11573−11580.
(26) Fang, X.; Chen, X.; Liu, Y.; Li, Q.; Zeng, Z.; Maiyalagan, T.; Mao, S. *ACS Appl. Nano Mater.* **2019**, *2*, 2367−2376.
(27) Roy, D.; Neogi, S.; De, S. *Chem. Eng. J.* **2022**, *428*, 131028.
(28) Jahan, M.; Bao, Q.; Loh, K. P. *J. Am. Chem. Soc.* **2012**, *134*, 6707−6713.
(29) Yao, B.; Chen, J.; Huang, L.; Zhou, Q.; Shi, G. *Adv. Mater.* **2016**, *28*, 1623−1629.
(30) Hu, X.; Xu, W.; Zhou, L.; Tan, Y.; Wang, Y.; Zhu, S.; Zhu, J. *Adv. Mater.* **2017**, *29*, 1604031.
(31) Li, C.; Jiang, D.; Liang, H.; Huo, B.; Liu, C.; Yang, W.; Liu, J. *Adv. Funct. Mater.* **2018**, *28*, 1704674.
(32) Wang, Y.; Wang, L.; Huang, W.; Zhang, T.; Hu, X.; Perman, J. A.; Ma, S. *J. Mater. Chem. A.* **2017**, *5*, 8385−8393.
(33) Xu, Z.; Yang, L.; Xu, C. *Anal. Chem.* **2015**, *87*, 3438−3444.
(34) Zhang, N.; Xu, Y.; Ma, Z. *Sens. Actuators, B.* **2020**, *317*, 128244.
(35) Ruan, X.; Liu, D.; Niu, X.; Wang, Y.; Simpson, C. D.; Cheng, N.; Du, D.; Lin, Y. *Anal. Chem.* **2019**, *91*, 13847−13854.
(36) Zhang, M.; Hu, X.; Mei, L.; Zhang, L.; Wang, X.; Liao, X.; Qiao, X.; Hong, C. *Microchem. J.* **2021**, *171*, 106870.
(37) He, B.; Dong, X. *Chem. Eng. J.* **2021**, *405*, 126642.
(38) Yin, H.; Ma, Q.; Zhou, Y.; Ai, S.; Zhu, L. *Electrochim. Acta* **2010**, *55*, 7102−7108.
(39) Wu, X.; Chai, Y.; Zhang, P.; Yuan, R. *ACS Appl. Mater. Interfaces* **2015**, *7*, 713−720.
(40) Nie, Y.; Yuan, X.; Zhang, P.; Chai, Y.-q.; Yuan, R. *Anal. Chem.* **2019**, *91*, 3452−3458.
(41) Zhu, D.; Liu, W.; Zhao, D.; Hao, Q.; Li, J.; Huang, J.; Shi, J.; Chao, J.; Su, S.; Wang, L. *ACS Appl. Mater. Interfaces* **2017**, *9*, 35597−35603.
(42) Wu, C.-j.; Huang, S.-q.; Wang, Y.-y.; Chai, Y.-q.; Yuan, R.; Yang, X. *Anal. Chem.* **2021**, *93*, 11019−11024.

(43) Zhao, Y.; Xiang, J.; Cheng, H.; Liu, X.; Li, F. *Biosens. Bioelectron.* **2021**, *194*, 113581.
(44) Xu, Z.-H.; Gao, H.; Zhang, N.; Zhao, W.; Cheng, Y.-X.; Xu, J.-J.; Chen, H.-Y. *Anal. Chem.* **2021**, *93*, 1686−1692.
(45) Li, X.; Li, X.; Li, D.; Zhao, M.; Wu, H.; Shen, B.; Liu, P.; Ding, S. *Biosens. Bioelectron.* **2020**, *168*, 112554.
(46) Luo, J.-H.; Li, Q.; Chen, S.-H.; Yuan, R. *ACS Appl. Mater. Interfaces* **2019**, *11*, 27363−27370.
(47) Zhu, L.; Zhang, X.; Chang, Y.; Xu, S.; Yuan, R.; Chai, Y. *Chem. Commun.* **2021**, *57*, 5179−5182.

https://doi.org/10.1021/acs.analchem.1c05293
Anal. Chem. 2022, 94, 5846−5855